Compositional Enhancement of Crustal Magnetization on Mars

A. Alhantoobi, J. Buz, J. O'Rourke, Benoit Langlais, C. Edwards

AGU ADVANCING EARTH AND SPACE SCIENCE

Geophysical Research Letters

RESEARCH LETTER
10.1029/2020GL090379

Compositional Enhancement of Crustal Magnetization on Mars

A. AlHantoobi[1], J. Buz[2], J. G. O'Rourke[3], B. Langlais[4], and C. S. Edwards[2]

[1]Aerospace Engineering Department, Khalifa University, Abu Dhabi, UAE, [2]Department of Astronomy and Planetary Sciences, Northern Arizona University, Flagstaff, AZ, USA, [3]School of Earth and Space Exploration, Arizona State University, Tempe, AZ, USA, [4]Laboratoire de Planétologie et Géodynamique, CNRS, Université de Nantes, Université d'Angers, Nantes, France

Key Points:

- The strong magnetization observed in the Terra Sirenum-Terra Cimmeria region is at least partially due to compositional enhancement
- The Terra Sirenum-Terra Cimmeria region has not experienced widespread demagnetization processes since formation
- The magnetization in the Terra Sirenum-Terra Cimmeria region is carried in the bulk rock with representative materials exposed at the surface

Supporting Information:

- Supporting Information S1

Correspondence to:

J. Buz,
jennifer.buz@nau.edu

Citation:

AlHantoobi, A., Buz, J., O'Rourke, J. G., Langlais, B., & Edwards, C. S. (2021). Compositional enhancement of crustal magnetization on Mars. *Geophysical Research Letters*, *48*, e2020GL090379. https://doi.org/10.1029/2020GL090379

Received 14 AUG 2020
Accepted 10 DEC 2020

Author Contributions:

Conceptualization: J. Buz
Formal analysis: A. AlHantoobi, J. Buz, J. G. O'Rourke
Funding acquisition: C. S. Edwards
Methodology: A. AlHantoobi, J. Buz, J. G. O'Rourke, B. Langlais, C. S. Edwards
Supervision: J. Buz, C. S. Edwards
Validation: A. AlHantoobi, J. Buz, J. G. O'Rourke, B. Langlais, C. S. Edwards

Abstract Martian orbital and lander measurements revealed strong (~1–2 orders of magnitude greater than Earth) crustal magnetic anomalies and the lack of an active detectable core dynamo. This strong crustal magnetization remains unexplained given that models of an ancient core dynamo on Mars predict surface field strengths comparable to modern Earth. We explored the relationship between Mars' crustal magnetization and its composition in multivariate space. We identified that 530 and 1,000 nm absorptions (from orbital spectrometers) have unique correlations with crustal magnetization in the Terra Sirenum-Terra Cimmeria region and ~13% of the variance of the magnetization can be attributed to these correlations. Because we do not expect the topmost material, detectable by the orbital spectrometers, to retain magnetization from an ancient core dynamo, we propose this material is compositionally similar to the bulk rock below it, which is more likely to retain magnetization. Therefore, the observed variance is a lower limit.

Plain Language Summary Currently Mars has no global magnetic field. However, at some point it did have a global magnetic field. Instruments from past missions have spotted patches on Mars' surface that are strongly magnetized. This can be explained by the fact that the crust was formed during a time when the global magnetic field was present, and so it locked in on that magnetic field. Previous models suggest that when Mars' global magnetic field was present, it was approximately of the same strength as Earth's current field. A magnetic field of this strength would not have produced such a strongly magnetized crust. Therefore, the magnetization strength of those patches is a mystery. We explored the relationships between the strength of the magnetic field on the surface and the composition of the crust. Our findings show that in the area with the strongest magnetic patches, there is a verifiable positive correlation between the magnetic field and mineralogical data. This leads us to believe that the composition of those patches enables them to record the magnetic field exceptionally well. Therefore, Mars' ancient global magnetic field did not need to be anomalously large to produce the strongly magnetized crust we observe.

1. Introduction

Satellite and ground-based measurements have demonstrated that Mars' ancient crust was magnetized during its formation and/or cooling and that currently there is no detectable core dynamo (Acuña et al., 1999; Connerney et al., 2004; Johnson et al., 2020). The geographic extent and uniformity of the magnetic field indicates that a steady ambient field persisted for at least a few hundred million years, implying an ancient internally generated magnetic field (Acuña et al., 1999). The Terra Sirenum-Terra Cimmeria (TSTC) region hosts particularly strong remanent magnetization, generating crustal fields predicted to be up to a few thousand nanotesla, more than an order of magnitude stronger than magnetic anomalies observed on other terrestrial planets or the Moon (Figure 1; Langlais et al., 2019). Possible explanations for the strongly magnetized crust in TSTC include one or more of the following: (1) a strong ancient magnetic field; (2) magnetized crust of a large depth/volume (3) magnetic minerals particularly well-suited for recording magnetization, for example, with a strong saturation magnetization; and/or (4) a magnetized unit with a lithology rich in magnetic minerals (Dunlop & Arkani-Hamed, 2005; Stevenson, 2001).

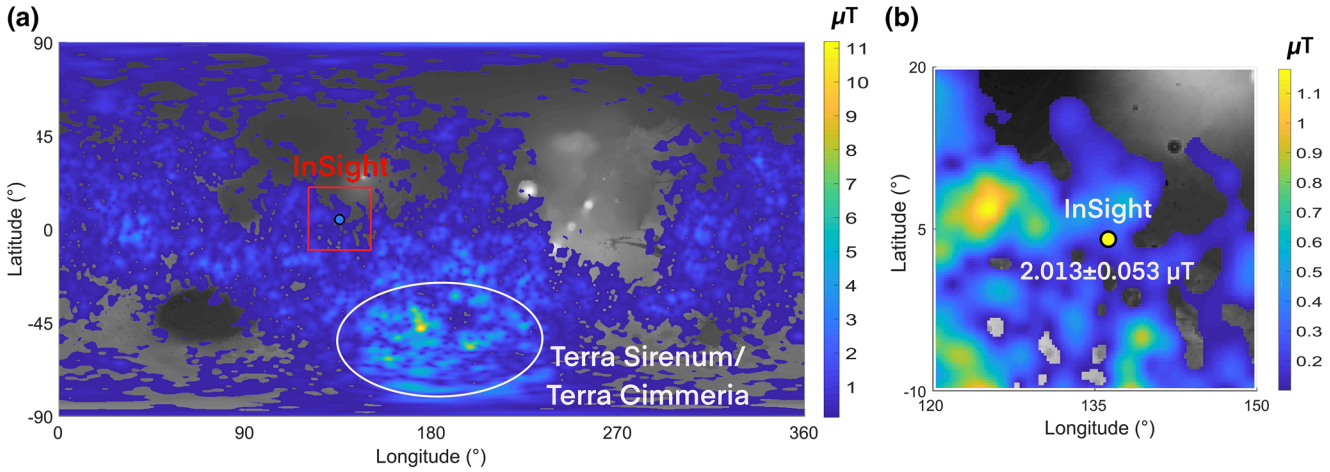

Figure 1. (a) Surface magnetic field prediction at 4 pixels/degree calculated using Langlais et al. (2019), regions where the predicted surface field was below 100 nT are excluded. Background is MOLA topography. (b) InSight result from Johnson et al. (2020) are shown above the predicted values.

Based on the measured magnetic field from orbit, at least 600 kA must be accounted for through the product of crustal volume and its vertically integrated magnetization (Dunlop & Arkani-Hamed, 2005). The areal extent of the magnetized region is known with the approximate precision of the satellite altitude (~100–200 km). The volume of the magnetized crust can be estimated by placing an upper-bound on the thickness of the magnetized layer based on the calculated depth to the Curie point isotherms (Connerney et al., 2001; Dunlop & Arkani-Hamed, 2005). Given the candidate magnetic phases (magnetite, hematite, maghemite, pyrrhotite, titanomagnetite, titanohematite, and, least likely, kamacite), the amount of magnetic material required ranges from 0.4 to 6 wt.% if the entire layer is magnetized (Dunlop & Arkani-Hamed, 2005). These proportions are consistent with measurements made on the Martian surface (e.g., Vaniman et al., 2014) and of some Martian meteorites (Gattacceca et al., 2014).

Recently, the magnetometer onboard InSight measured a surface magnetic field nearly 10X stronger than modeled by previous satellite-based observations (Figure 1; Johnson et al., 2020; Langlais et al., 2019; Morschhauser et al., 2014). This observation is not entirely unexpected as smaller (below orbital resolution), local variations are expected. Yet, the potential contribution from local variations does not fully explain the strength and cohesiveness of magnetic fields detected above Mars in the TSTC region.

Both modeling and paleointensity estimates from Martian meteorites yield ancient Martian magnetic field strengths on the order of Earth's current field (~50 μT) (Stevenson, 2001; Weiss et al., 2008). Furthermore, a mechanism for generating fields much stronger than this given Mars' density, rotation rate, and conductivity is currently unknown (Stevenson, 2001), making explanation (1) unlikely. We explore explanations (2)–(4).

2. Methods

2.1. Data Sets

Predictions of surface magnetic field assessed in this study are derived from a model of the crustal magnetic field of Mars which combines measurements from the Mars Global Surveyor (MGS) and Mars Atmosphere and Volatile EvolutioN (MAVEN) magnetometer (Langlais et al., 2019). The data sets used for comparison included elemental maps from the Gamma Ray Spectrometer (GRS) (Boynton et al., 2004), mineralogical parameters from Compact Reconnaissance Imaging Spectrometer for Mars (CRISM), Observatoire pour la Mineralogie, l'Eau, les Glaces et l'Activité (OMEGA), and the Thermal Emission Spectrometer (TES), as well as TES-derived surface types. A summary of the data sets used, their resolution, and coverage are provided in Table 1.

Table 1
Data Products

Data product	Instrument	References	Data set resolution (Equatorial resolution in km)	Instrument resolution	Coverage
Crustal magnetic field model	Magnetometer (MAVEN), Mag/Electron Reflectometer (MGS)	Langlais et al. (2019)	1 px/0.25°* (~15 km)*model predictions	N/A	Full
Elemental concentration	GRS	Boynton et al. (2007); Karunatillake et al. (2016)	1 px/5° (~295 km)		Full between ±60° latitude
Fe				267 km	
Si				219 km	
K				215 km	
S				~230 km	
Al				~230 km	
Ca				~230 km	
Cl				217 km	
H				222 km	
Th				240 km	
Mineral abundances	TES	Bandfield (2002)	1 px/0.25° (~15 km)	16 km	Full
Quartz (Qtz)					
K-Feldspar (Kspar)					
Plagioclase (Plag)					
Amphibole (Amph)					
Low-Ca Pyroxene (LCP)					
High-Ca Pyroxene (HCP)					
Olivine (Ol)					
Hematite (Hem)					
Sulfates (Sulf)					
Carbonates (Carb)					
Phyllosilicates (Phyll)					
Rock type abundance	TES	Bandfield et al. (2000)	1 px/0.25° (~15 km)	16 km	Full
Basalt (ST1)					
Andesite (ST2)					
1,000-nm band depth infrared contribution (BDI1000IR)	CRISM	Viviano-Beck et al. (2014)	1 px/0.015° *	100–200 m	94%
1,000 nm band depth visible contribution (BDI100VIS)			*binned at 25% resolution to reduce data volume issues		
High-Ca Pyroxene Index (HCPINDEX)					
Low-Ca Pyroxene Index (LCPINDEX)					
Olivine Index (OLINDEX)					
530-nm band depth (BD530)	OMEGA	Ody et al. (2012)	1 px/0.025° (~1.5 km)	2 km	90%
2,000-nm band depth (BD2000)					
Nanophase Iron (NNPH)					
Thermal inertia	TES	Putzig and Mellon (2007)	1 px/0.05° (~3 km)	7.5 km	Full
Lambert albedo (LA)	TES	Christensen et al. (2001)	1 px/0.25° (~15 km)	16 km	Full
Dust cover index	TES	Ruff and Christensen(2002)	1 px/0.25° (~15 km)	16 km	Full

2.2. Statistical Analysis

There are many covarying relationships between crustal properties. Considering two variables at a time in bivariate analysis can create misleading apparent correlations (Karunatillake et al., 2012). To accurately compare these disparate data sets, we applied a multivariate correlation and regression methodology similar to that of Karunatillake et al. (2012) with magnetic field model result as the response variable and compositional data sets as the predictor variables. We used two distinct yet complementary multivariate analysis methods of Karunatillake et al. (2012)—ordinary linear regression (OLR) and spatially weighted linear regression (SWLR)—to estimate the correlation between the magnetic field model and our predictor variables (all other data sets). OLR estimates the partial correlation of the magnetic field with each predictor variable. SWLR modifies the OLR method to account for spatial autocorrelation. The multivariate analysis methods help to verify the significance of observed correlations in the bivariate analysis and can reveal correlations that were not initially apparent.

We calculated the Langlais crustal magnetic field model (Langlais et al., 2019) at a resolution matching that of TES. We then trimmed the geographic extent of each data set to match the most limited footprint and sampled each data set to match the resolution of the lowest-resolution data set. Finally, we excluded regions where the predicted surface magnetic field was below 100 nT (Figure 1) and where TES lambert albedo was above 0.2 (to avoid extensive dust cover).

Full equations and methods are available in Karunatillake et al. (2012) and references therein with differences in Section S1 (supporting information). The variance contribution, R^2, is a numeric value between 0 and 1 that represents the fraction of the response variance attributable to the predictors in each method. The partial correlation coefficient, r_i, indicates the unique correlation between the response variable and the individual data set. To verify if the methods are sufficiently robust for the data, we use the expected R^2 if the response were uncorrelated with any of the predictors (R_0^2) and R^2 adjusted for the degrees of freedom (R_{df}^2). If R_0^2 exceeds 0.1 or R_{df}^2 is less than 0.1, then any apparent correlation can be considered insignificant. To assess the significance of the correlation estimates, we used the *p*-value from the Student's *t*-test distribution for OLR and standard normal probability distribution for SWLR to eliminate predictors that fail to meet the 95% confidence threshold. Univariate (OLR and SWLR) and Bonferroni (OLR) confidence intervals were computed. Predictor variables with confidence intervals that include zero (indicating very minimal/no significant correlation between the response and the predictor) were eliminated. Any analysis that revealed key predictor variables through OLR was then subjected to SWLR. Predictor variables with contributions >0.05 were considered key predictors.

SWLR analysis requires quantifying the degree to which individual bins are distinct from neighboring bins. Additionally, spatial weighting due to map projections and sampling differences at the poles and equator is incorporated. To define a spatial weighting matrix, we plotted the similarity function for all our data sets. This function allowed us to determine the similarity between values of bin pairs at given angular separation. Beyond a threshold angular separation, the similarity value remains constant. This threshold angular separation can then be used to find the constant of decay for bin similarity. We obtained the constant of decay for the highest threshold angular separation to ensure that spatial autocorrelation has been accounted for across all predictors. The *"Model σ"* is the uncertainty of the overall spatial autocorrelation fit, "ρ" is a scalar of the spatial weights matrix determined by the similarity function and "C" is the constant of regression.

We first attempted multivariate analysis at the lowest resolution data set (GRS), which enabled the inclusion of all data sets. The geographic extent and large footprint of GRS resulted in too few datapoints for analysis. These results are further discussed in Section S2 (supporting information). OLR and SWLR were then applied at the second lowest resolution (TES) with the goal of reducing the number of predictors and simultaneously avoiding degradation of the potential variance contribution as a result of binning. Analyses were conducted both on global and regional scales.

For regional analyses, we used the compositional provinces identified by Gasnault et al. (2010) and Rogers and Hamilton (2015) and geologic units mapped by Tanaka et al. (2014). Individual geologic units are quite small for robust statistics, so geologic units of similar age were also grouped and analyzed. Results of these analyses did not yield meaningful correlations and are discussed in Section S2 (supporting information).

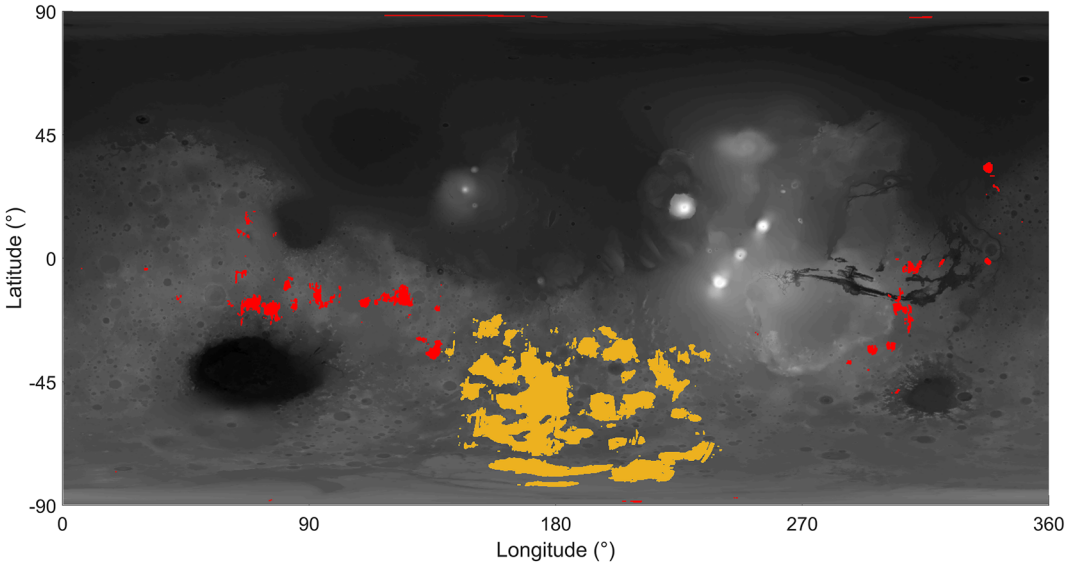

Figure 2. Mars orbiter laser altimeter topography with yellow indicating the region of interest and red indicating discarded points outside of TSTC.

2.3. Analysis at TSTC

We conducted additional analyses on the region of maximum crustal magnetization, TSCS. The maximum field in this region is > 11 μT at the surface as predicted by the global model (Langlais et al., 2019). To define the exact region of interest, we generated scatter plots between the predicted magnetic field and the ferric mineral indicators. Those that show a positively correlated trend within the global distribution were chosen (Figure S1), mainly the 530 nm band depth (BD530) and nanophase iron spectral parameter (NNPH). The data sets were normalized and each point on the graph was assigned a slope value relative to the origin. We then selected a range of slope values and captured all the points that lie within the range. The slopes selected for BD530 ranged between 0.4 and 1.2 and those of NNPH between 0.6 and 1.6. Furthermore, we excluded parameter values that were within 10% of the minimum value and magnetic field values that were below 400 nT (to exclude transitional areas between positively and negatively magnetized regions). The remaining points from both scatter plots were then combined into one mask and points outside of TSTC were discarded (Figure 2).

3. Results

A scatter plot matrix of points within the region of interest (n = 19,133) was generated (Figure S1). This initial bivariate analysis reveals that the 530 nm band depth (BD530), NNPH, lambert albedo, and thermal inertia (TI) all show potential positive correlation while high calcium pyroxene (HCP), 2,000-nm band depth (BD2000), 1,000-nm band depth (BDI1000), and surface type 1 abundance all show potential negative correlation (see Table 2). Importantly, the bivariate analysis results are not considered of significance until they are verified using the multivariate OLR and SWLR methods.

Table 2
Key Predictor Variables

Method	Key predictors	Rejected predictors	Variance contribution
Scatter Plots	Hcp, BD530, NNPH, BD2000, BD1000IR, LA, ST1, TI	Amph, Carb, Dust, Hem, Kspar, Lcp, OL, Phyll, Plag, Qtz, Sulf, BD1000VIS, LCP Index, OL Index, ST2	–
OLR	BD530, BD2000, BD1000VIS, TI	Amph, Hcp, LCP, Phyll, Plag, Qtz, LCP Index, ST1, ST2	16.69%
SWLR	BD530, BD1000VIS	Amph, Carb, Dust, Hcp, Hem, Phyll, Plag, Qtz, ST2, TI	13.56%

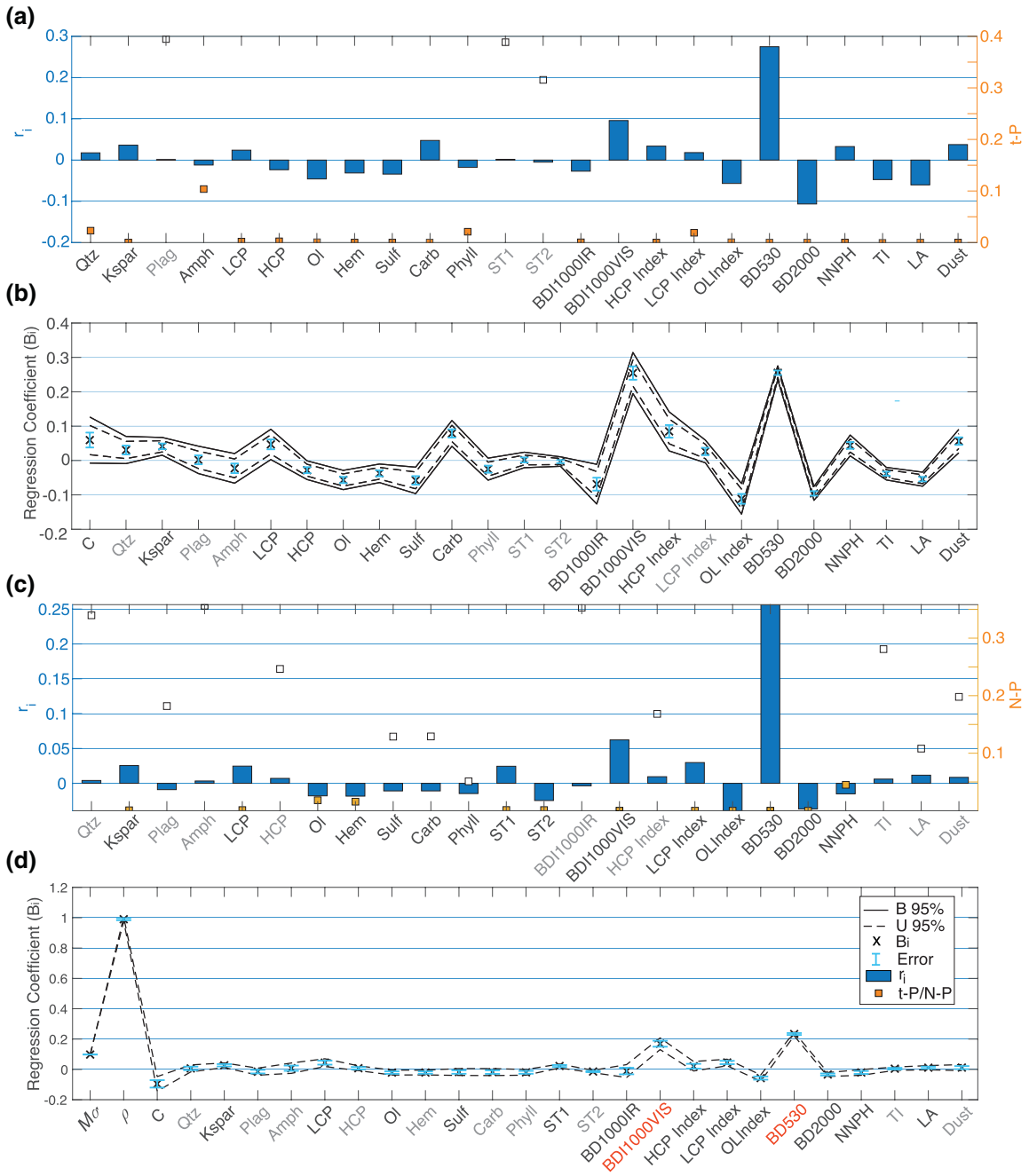

Figure 3. (a) OLR correlation results. Solid blue columns represent the unique correlations (r_i) between the predictors (data sets) and the response (magnetic field model). *t-P* is the probability that r_i could be as extreme as the one obtained by the analysis, when sampled from an uncorrelated population. Predictors that pass the *t-P* 95% confidence threshold are filled, while the rest are empty. (b) OLR regression. B_i are the regression coefficients with error bars at one standard error. The variable *"C"* is the constant of regression. Solid and dashed black lines are Bonferroni and univariate 95% confidence intervals, respectively. A predictor passes the test if both confidence intervals do not include zero. Predictors that pass with significant contribution (>0.05) are in red. (c) SWLR correlation results. *N-P* is the Gaussian analog to *t-P* used in the OLR analysis. (d) SWLR regression results.

Using OLR analysis, many predictor variables indicate unique correlations with magnetic field (Figure 3a). Several predictor variables have confidence intervals that do not include zero and therefore pass both the univariate and Bonferroni confidence intervals (Figure 3b). The variance contribution from this analysis indicates that ~17% of change in the magnetic field can be linked to changes in the predictor variables. Table 2 summarizes these results.

The maximum threshold angular separation, after which there is insignificant contribution from neighboring bins, is 72°. Using these threshold angular separations, we were able to determine the spatial weighting matrix for SWLR analysis. As expected, fewer predictor variables pass this analysis with significance (see Figure 3c, Table 2). Of the predictor variables that pass, only two do so with significant contribution (>0.05; Figure 3d). The variance contribution from this analysis indicates that ~13% of the change in magnetic field can be linked to changes within these variables, primarily from BD530 and BDI1000VIS.

4. Discussion

4.1. Meaning of Key Predictors

Although several predictor variables pass our SWLR analysis, only BD530 and BDI1000VIS contribute more than 0.05% to the variance contribution. Both indicators are related to iron bearing mineral phases (Ody et al., 2012; Viviano-Beck et al., 2014) and therefore potentially sensitive to magnetic phases. BD530, associated with absorptions at 530-nm, has been attributed to multiple spectroscopic effects from Fe^{3+} while BDI1000VIS, a broad absorption at 1-μm, is typically associated with electronic transitions and charge transfer absorptions from iron in the crystal structure of olivine and pyroxene or from Fe-bearing glass. Vis-NIR reflectance for four candidate magnetic phases from the USGS spectral library (Clark et al., 2007) and the calculation of their parameters is shown in Figure S2. Our statistical analysis does not indicate which magnetic phases are most likely.

Different iron-rich minerals have distinct susceptibilities to remanent magnetization. Magnetite, pyrrhotite, and hematite have all been proposed as magnetic carriers on Mars (Dunlop & Arkani-Hamed, 2005; Gattacceca et al., 2014; Kletetschka et al., 2000; McEnroe et al., 2004a; McEnroe et al., 2004b; Nimmo, 2000). Previous studies assumed that the magnetized layer in TSTC began at ~10 km depth and continued downwards until the Curie point(s) of the magnetic mineral(s) were reached (Dunlop & Arkani-Hamed, 2005; McEnroe et al., 2018). For example, ~0.8 wt.% of single-domain magnetite in a ~30–40-km thick layer could produce the necessary vertically integrated magnetization of ~600 kA. However, recent results from the NASA InSight Mission (Johnson et al., 2020) and new MAVEN data (Mittelholz et al., 2020) show that some magnetized layers on Mars could be thin and/or shallowly buried (~200 m–10 km). Figure S5 illustrates that thin layers of magnetized crust (<2-km thick) can produce the predicted magnetic fields at TSTC if roughly one third of the iron (>10 wt.% from GRS data) is in the form of single-domain magnetite and/or pyrrhotite (using an average density for the bulk crust of 2,900 kg/m^3; Zuber, 2001). Other minerals (hematite, maghemite, and/or multidomain magnetite) are only credible candidates for the primary magnetic carrier(s) if the magnetized layer is >10–20-km thick (Section S3, Table S1, supporting information).

4.2. Local Compositional Enhancement of Magnetization

The variance contribution from BD530 and BD1000VIS indicates that composition of the crust influences its magnetization. Using the data sets available for this study, we can account for ~13% of the variance in magnetic field. It is important to consider the sensitivity of the instruments we used for comparison with magnetic field are only sensitive to the top ~50 μm (TES) or top ~ few μm (CRISM and OMEGA). This uppermost material has likely undergone some combination of erosion, alteration, impact cratering, or other process which removed any magnetization from an ancient dynamo. Instead, the magnetization detected from orbit likely originates in either the bulk rock or within deeper layers of similar composition, which are more likely to preserve remanence from an ancient dynamo. This interpretation is consistent with the measurements observed at the InSight landing site (Johnson et al., 2020) and Lucus Planum (Mittelholz et al., 2020) in which the magnetization is carried in comparatively shallow layers, contrary to previous magnetic source depth models (Dunlop & Arkani-Hamed, 2005; Lewis & Simons, 2012). We have applied our statistical analysis at Lucus Planum and found that at least 7% of the variance contribution to predicted magnetic field can be explained through mineralogy (Figure S3).

Geological mapping in the TSTC region (Tanaka et al., 2014) indicates that the majority of the exposed material is a Noachian highland unit, which in our analysis is exposed within a ~6-km deposit (Figure S4). In

order to explain the correlation between surface composition and bulk or buried magnetization, there must be compositional similarity between the uppermost material in TSTC and the layers that retain remanent magnetization. Our preferred explanation is that the uppermost material is derived from the bulk rock, which carries the magnetization. This assumption is further validated by the recent crustal magnetism analysis at Lucus Planum which has shown magnetization carried within an upper unit (Mittelholz et al., 2020). Using estimates for the lifetime of the ancient dynamo (Moore & Bloxham, 2017; Roberts et al., 2009), we can expect that the majority of the remanence is carried in the early and middle Noachian units mapped by Tanaka et al. (2014) in TSTC. Other possible explanations are iron-enrichments resulting from hydrothermal alteration or dike emplacement. However, these later deposits/intrusions must be large enough to produce an observable signal in the remote sensing data taken of the surface, and therefore we consider them less likely sources of the predicted magnetic field. In all scenarios, the observation of mineralogy correlated with magnetization remains.

The variance contribution is likely an underestimate of the compositional enhancement in TSTC. Any portion of our region of interest which lost its magnetic remanence, such as the uppermost material discussed above, would have the effect of reducing the variance contribution we observe because it would be uncorrelated but interspersed within the correlated data. Therefore, the positive correlations we observe indicate that without this compositional influence the intensity of the crustal magnetization would be reduced. As previously discussed, the magnitude of Mars' crustal magnetization has previously conflicted with current models for the strength of potential ancient core dynamos (e.g., Stevenson, 2001). This result reduces the discrepancy between models of ancient field strength and crustal magnetization.

In addition to the compositional enhancements observed through this analysis, there are broad implications for the history of the TSTC region. The correlation we observe between composition and magnetization suggests that the surface material in TSTC is locally sourced and has not mixed significantly with global regolith. Tanaka et al. (2014) indicate that this region primarily consists of Noachian-aged units ranging in thickness between hundreds of meters to a few kilometers. Therefore, TSTC as a whole has remained largely unaffected by demagnetizing processes since the Noachian.

5. Conclusion

Our analysis indicates that in the TSTC region on Mars, the strong magnetization is at least partially due to compositional (iron) enhancements and not necessarily solely from a strong paleofield. This finding significantly reduces the discrepancy between models of ancient field strength and crustal magnetization and suggests that Mars' ancient paleofield does not need to be of exceptionally high strength. This work places additional constraints on the depth and thickness of the magnetized layer and/or the amount of magnetized minerals and is consistent with previous findings related to Mars crustal magnetic mineralogy (Dunlop & Arkani-Hamed, 2005; e.g., Kletetschka et al., 2000). For example, two possible scenarios are (1) <2-km thick layer containing minerals with high saturation magnetization (such as single domain magnetite and/or pyrrhotite), or (2) a > 10–20-km thick layer with minerals of weaker saturation magnetization (such as hematite and/or maghemite). When considered with other recent results (e.g., Johnson et al., 2020; Mittelholz et al., 2020), much of Mars' crustal magnetization can be explained by shallow and/or thin layers of magnetized material, dramatically different from early models (e.g., Connerney et al., 1999). Finally, heating or other demagnetizing processes must be absent at large scales in TSTC for the magnetization to be coherent (consistent with Bouley et al. (2020)). The uppermost material (<10 μm) in TSTC is compositionally similar to the bulk rock, which retains the magnetization, indicating it is recently eroded or locally sourced.

Data Availability Statement

All data sets used in this work are available through JMARS (https://jmars.mars.asu.edu/) or the NASA Planetary Data System (PDS) (https://pds-geosciences.wustl.edu/dataserv/mars.html). The Mars Odyssey Gamma Ray Spectrometer (GRS) derived chemical maps were derived from the spectral data archived on the PDS by applying the spectra-to-chemistry modeling methods described by Boynton et al. (2007), Evans et al. (2006), and Karunatillake et al. (2007). The derived chemical maps have also been described and analyzed in the works by Hood et al. (2019) and Ojha et al. (2019), among others.

Acknowledgments
We would like to thank the JMARS team for providing global data sets, and Deanne Rogers and Olivier Gasnault for their compositional provinces maps. We thank Suniti Karunitillake for assistance and verification of the multivariate analysis methods. Our analyses were made possible through the use of the NAU Monsoon High Performance Computing cluster. This research was funded in part through a collaboration between the Mohammed Bin Rashid Space Centre, Northern Arizona University, and the University of Colorado, Boulder Laboratory for Atmospheric and Space Physics and the 2001 Mars Odyssey Project.

References

Acuña, M. H., Connerney, J. E. P., Ness, N. F., Lin, R. P., Mitchell, D., Carlson, C. W., et al. (1999). Global distribution of crustal magnetization discovered by the mars global surveyor MAG/ER experiment. *Science*, *284*(5415), 790–793. https://doi.org/10.1126/science.284.5415.790

Bandfield, J. L. (2002). Global mineral distributions on Mars. *Journal of Geophysical Research*, *107*(E6), 1–9. https://doi.org/Artn504210.1029/2001je001510

Bandfield, J. L., Hamilton, V. E., & Christensen, P. R. (2000). A global view of Martian surface compositions from MGS-TES. *Science*, *287*(5458), 1626–1630. https://doi.org/10.1126/science.287.5458.1626

Bouley, S., Keane, J. T., Baratoux, D., Langlais, B., Matsuyama, I., Costard, F., et al. (2020). A thick crustal block revealed by reconstructions of early Mars highlands. *Nature Geoscience*, *13*(2), 105–109. https://doi.org/10.1038/s41561-019-0512-6

Boynton, W. V., Feldman, W. C., Mitrofanov, I. G., Evans, L. G., Reedy, R. C., Squyres, S. W., et al. (2004). The Mars Odyssey Gamma-Ray Spectrometer Instrument Suite. In C. T. Russell (Ed.), *2001 Mars Odyssey* (pp. 37–83). Dordrecht: Springer Netherlands. https://doi.org/10.1007/978-0-306-48600-5_2

Boynton, W. V., Taylor, G. J., Evans, L. G., Reedy, R. C., Starr, R., Janes, D. M., et al. (2007). Concentration of H, Si, Cl, K, Fe, and Th in the low- and mid-latitude regions of Mars. *Journal of Geophysical Research*, *112*, E12S99. https://doi.org/10.1029/2007JE002887

Christensen, P. R., Bandfield, J. L., Hamilton, V. E., Ruff, S. W., Kieffer, H. H., Titus, T. N., et al. (2001). Mars Global Surveyor Thermal Emission Spectrometer experiment: Investigation description and surface science results. *Journal of Geophysical Research: Planets*, *106*(E10), 23823–23871. https://doi.org/10.1029/2000JE001370

Clark, R. N., Swayze, G. A., Wise, R., Livo, K. E., Hoefen, T. M., Kokaly, R. F., & Sutley, S. J. (2007). *USGS digital spectral library splib06a*. Reston, VA: US Geological Survey.

Connerney, J. E. P., Acuña, M. H., Ness, N. F., Spohn, T., & Schubert, G. (2004). Mars Crustal Magnetism BT - Mars' Magnetism and Its Interaction with the Solar Wind. In D. Winterhalter, M. Acuña & A. Zakharov (Eds.), (pp. 1–32). Dordrecht: Springer Netherlands. https://doi.org/10.1007/978-0-306-48604-3_1

Connerney, J. E. P., Acuña, M. H., Wasilewski, P. J., Kletetschka, G., Ness, N. F., Rème, H., et al. (2001). The global magnetic field of Mars and implications for crustal evolution. *Geophysical Research Letters*, *28*(21), 4015–4018. https://doi.org/10.1029/2001GL013619

Connerney, J. E. P., Acuña, M. H., Wasilewski, P. J., Ness, N. F., Reme, H., Mazelle, C., et al. (1999). Magnetic lineations in the ancient crust of Mars. *Science*, *284*(5415), 794–798. https://doi.org/10.1126/science.284.5415.794

Dunlop, D. J. J., & Arkani-Hamed, J. (2005). Magnetic minerals in the Martian crust. *Journal of Geophysical Research*, *110*(E12), 1–11. https://doi.org/10.1029/2005JE002404

Evans, L. G., Reedy, R. C., Starr, R. D., Kerry, K. E., & Boynton, W. V. (2006). Analysis of gamma ray spectra measured by Mars Odyssey. *Journal of Geophysical Research*, *111*, E03S04. https://doi.org/10.1029/2005JE002657

Gasnault, O., Jeffrey Taylor, G., Karunatillake, S., Dohm, J., Newsom, H., Forni, O., et al. (2010). Quantitative geochemical mapping of martian elemental provinces. *Icarus*, *207*(1), 226–247. https://doi.org/10.1016/j.icarus.2009.11.010

Gattacceca, J., Rochette, P., Scorzelli, R. B., Munayco, P., Agee, C. B., Quesnel, Y., et al. (2014). Martian meteorites and Martian magnetic anomalies: A new perspective from NWA 7034. *Geophysical Research Letters*, *41*(14), 4859–4864. https://doi.org/10.1002/2014gl060464

Hood, D. R., Karunatillake, S., Gasnault, O., Williams, A. J., Dutrow, B., Ojha, L., et al. (2019). Contrasting regional soil alteration across the topographic dichotomy of Mars. *Geophysical Research Letters*, *46*(23), 13668–13677. https://doi.org/10.1029/2019GL084483

Johnson, C. L., Mittelholz, A., Langlais, B., Russell, C. T., Ansan, V., Banfield, D., et al. (2020). Crustal and time-varying magnetic fields at the InSight landing site on Mars. *Nature Geoscience*, *13*(3), 199–204. https://doi.org/10.1038/s41561-020-0537-x

Karunatillake, S., Gasnault, O., Squyres, S. W., Keller, J. M., Janes, D. M., Boynton, W., & Newsom, H. E. (2012). Martian case study of multivariate correlation and regression with planetary datasets. *Earth, Moon, and Planets*, *108*(3–4), 253–273.

Karunatillake, S., Keller, J. M., Squyres, S. W., Boynton, W. V., Brückner, J., Janes, D. M., et al. (2007). Chemical compositions at Mars landing sites subject to Mars Odyssey Gamma Ray Spectrometer constraints. *Journal of Geophysical Research*, *112*, E08S90. https://doi.org/10.1029/2006JE002859

Karunatillake, S., Wray, J. J., Gasnault, O., McLennan, S. M., Deanne Rogers, A., Squyres, S. W., et al. (2016). The association of hydrogen with sulfur on Mars across latitudes, longitudes, and compositional extremes. *Journal of Geophysical Research: Planets*, *121*(7), 1321–1341. https://doi.org/10.1002/2016JE005016

Kletetschka, G., Wasilewski, P. J., & Taylor, P. T. (2000). Mineralogy of the sources for magnetic anomalies on Mars. *Meteoritics & Planetary Sciences*, *35*(5), 895–899. https://doi.org/10.1111/j.1945-5100.2000.tb01478.x

Langlais, B., Thébault, E., Houliez, A., Purucker, M. E., & Lillis, R. J. (2019). A New Model of the Crustal Magnetic Field of Mars Using MGS and MAVEN. *Journal of Geophysical Research: Planets*, *124*(6), 1542–1569. https://doi.org/10.1029/2018JE005854

Lewis, K. W., & Simons, F. J. (2012). Local spectral variability and the origin of the Martian crustal magnetic field. *Geophysical Research Letters*, *39*, L18201. https://doi.org/10.1029/2012GL052708

McEnroe, S. A., Brown, L. L., & Robinson, P. (2004a). Earth analog for Martian magnetic anomalies: Remanence properties of hemo-ilmenite norites in the Bjerkreim-Sokndal intrusion, Rogaland, Norway. *Journal of Applied Geophysics*, *56*(3), 195–212. https://doi.org/10.1016/S0926-9851(04)00052-7

McEnroe, S. A., Robinson, P., Church, N., & Purucker, M. (2018). Magnetism at depth: A view from an ancient continental subduction and collision zone. *Geochemistry, Geophysics, Geosystems*, *19*(4), 1123–1147. https://doi.org/10.1002/2017GC007344

McEnroe, S. A., Skilbrei, J. R., Robinson, P., Heidelbach, F., Langenhorst, F., & Brown, L. L. (2004b). Magnetic anomalies, layered intrusions and Mars. *Geophysical Research Letters*, *31*(19), 31–34. https://doi.org/10.1029/2004GL020640

Mittelholz, A., Johnson, C. L., Feinberg, J. M., Langlais, B., & Phillips, R. J. (2020). Timing of the Martian dynamo: New constraints for a core field 4.5 and 3.7 Ga ago. *Science Advances*, *6*(18), eaba0513. https://doi.org/10.1126/sciadv.aba0513

Moore, K. M., & Bloxham, J. (2017). The construction of sparse models of Mars's crustal magnetic field. *Journal of Geophysical Research: Planets*, *122*(7), 1443–1457. https://doi.org/10.1002/2016JE005238

Morschhauser, A., Lesur, V., & Grott, M. (2014). A spherical harmonic model of the lithospheric magnetic field of Mars. *Journal of Geophysical Research: Planets*, *119*(6), 1162–1188. https://doi.org/10.1002/2013JE004555

Nimmo, F. (2000). Dike intrusion as a possible cause of linear Martian magnetic anomalies. *Geology*, *28*(5), 391–394. https://doi.org/10.1130/0091-7613(2000)028<0391:DIAAPC>2.3.CO;2

Ody, A., Poulet, F., Langevin, Y., Bibring, J.-P., Bellucci, G., Altieri, F., et al. (2012). Global maps of anhydrous minerals at the surface of Mars from OMEGA/MEx. *Journal of Geophysical Research*, *117*, E00J14. https://doi.org/10.1029/2012JE004117

Ojha, L., Karunatillake, S., & Iacovino, K. (2019). Atmospheric injection of sulfur from the Medusae Fossae forming events. *Planetary and Space Science*, *179*, 104734. https://doi.org/10.1016/j.pss.2019.104734

Putzig, N. E., & Mellon, M. T. (2007). Apparent thermal inertia and the surface heterogeneity of Mars. *Icarus*, *191*(1), 68–94. https://doi.org/10.1016/j.icarus.2007.05.013

Roberts, J. H., Lillis, R. J., & Manga, M. (2009). Giant impacts on early mars and the cessation of the Martian dynamo. *Journal of Geophysical Research*, *114*(4), 1–10. https://doi.org/10.1029/2008JE003287

Rogers, A. D., & Hamilton, V. E. (2015). Compositional provinces of Mars from statistical analyses of TES, GRS, OMEGA and CRISM data. *Journal of Geophysical Research: Planets*, *120*(1), 62–91. https://doi.org/10.1002/2014JE004690

Ruff, S. W., & Christensen, P. R. (2002). Bright and dark regions on Mars: Particle size and mineralogical characteristics based on Thermal Emission Spectrometer data. *Journal of Geophysical Research: Planets*, *107*(E12), 2–22. https://doi.org/10.1029/2001JE001580

Stevenson, D. J. (2001). Mars' core and magnetism. *Nature*, *412*(6843), 214–219. https://doi.org/10.1038/35084155

Tanaka, K. L., Robbins, S. J., Fortezzo, C. M., Skinner, J. A., & Hare, T. M. (2014). The digital global geologic map of Mars: Chronostratigraphic ages, topographic and crater morphologic characteristics, and updated resurfacing history. *Planetary and Space Science*, *95*, 11–24. https://doi.org/10.1016/j.pss.2013.03.006

Vaniman, D. T., Bish, D. L., Ming, D. W., Bristow, T. F., Morris, R. V., Blake, D. F., et al. (2014). Mineralogy of a mudstone at Yellowknife Bay, Gale crater, Mars. *Science*, *343*(6169), 1243480. https://doi.org/10.1126/science.1243480

Viviano-Beck, C. E., Seelos, F. P., Murchie, S. L., Kahn, E. G., Seelos, K. D., Taylor, H. W., et al. (2014). Revised CRISM spectral parameters and summary products based on the currently detected mineral diversity on Mars. *Journal of Geophysical Research: Planets*, *119*(6), 1403–1431. https://doi.org/10.1002/2014je004627

Weiss, B. P., Fong, L. E., Vali, H., Lima, E. A., & Baudenbacher, F. J. (2008). Paleointensity of the ancient Martian magnetic field. *Geophysical Research Letters*, *35*(23), https://doi.org/10.1029/2008gl035585

Zuber, M. T. (2001). The crust and mantle of Mars. *Nature*, *412*(6843), 220–227. https://doi.org/10.1038/35084163